Simulations of Photodegradation of Toluene and Formaldehyde in a Monolith Reactor Using Computational Fluid Dynamics

Siewhui Chong, Shaobin Wang, Moses Tadé, H. Ming Ang, and Vishnu Pareek
Dept. of Chemical Engineering, CRC for Contamination Assessment and Remediation of the Environment,
Curtin University of Technology, Perth, WA 6845, Australia

DOI 10.1002/aic.12295

In this study, simulations were conducted on a monolith reactor for the photodegradation of toluene and formaldehyde. The monoliths in the reactor were treated as porous zones and the photocatalytic oxidation occurring on the monolith surfaces was modeled using Langmuir–Hinshelwood kinetics. A discrete ordinates model was used to simulate the light intensity with a novel approach, which involved an adjustable parameter—the absorption coefficient of the channel wall, for modeling the local light intensity across the porous media. The advantage of this approach was that despite its simplicity, it was able to capture and visualize the local light profile across the monolith channels and to integrate it into the reaction kinetics. Although it required a trial-and-error to determine the correct value of the channel wall absorption coefficient, the proposed model achieved a reasonable agreement between the simulation results and published experimental data. © 2010 American Institute of Chemical Engineers *AIChE J,* 57: 724–734, 2011

Keywords: CFD, porous, photocatalytic oxidation, monolith, discrete ordinates

Introduction

"Sick Building Syndrome" is caused by long-term exposure to air toxics consisting mostly of volatile organic compounds (VOCs) in indoor air which has been known to be carcinogenic to human health.[1,2] The buildings that contain air toxics coming from the paintings, carpeting, building materials, office equipments, etc., are known as the "sick buildings." Sick-building syndromes are such as dizziness, dry or itchy skin, eye, nose and throat irritation, a dry cough, fatigue, headache, increased rate, or asthma attack and reduced concentration.[2–4] Most of the syndromes are caused by poor air quality, which is mostly due to inadequate heating-ventilation-air-conditioning (HVAC) system in the buildings.[2,3] To prevent the sick building syndromes, improving the indoor air quality has become a crucial issue. In the past, there have been a number of conventional methods for air purification, such as the thermal and catalytic oxidation, adsorption and condensation.[5] However, these methods are costly as they need higher operating temperatures and pressures, catalyst regeneration or waste handling.[6] Heterogeneous photocatalytic oxidation technology, on the other hand, appears to be a more practical and promising alternative to the conventional methods for its ability to operate under ambient conditions.[4] In a photoreactor, VOCs are adsorbed onto the surface of the photocatalyst, and oxidized by the OH radicals formed by the photocatalyst in the presence of UV radiation. The common photocatalyst is titanium dioxide because of its low cost, high-refractive index, and strong oxidative potential.[3]

There are several designs of photocatalytic reactors for air purification such as annular packed bed,[7] honeycomb monolith,[8,9] optical-fiber,[10–13] and photo-CREC-air.[14] These

---

Correspondence concerning this article should be addressed to V. Pareek at v.pareek@curtin.edu.au.

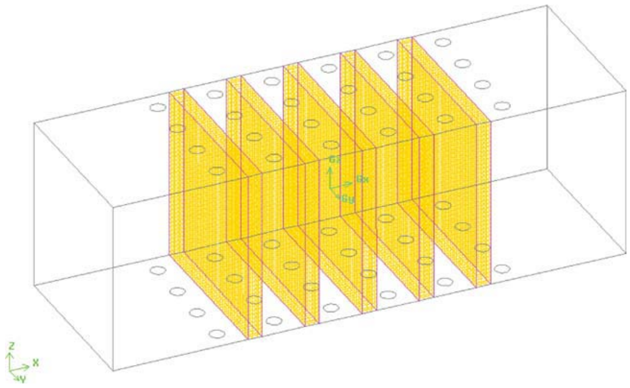

Figure 1. Monolith photoreactor with five monoliths and six lamp banks.

[Color figure can be viewed in the online issue, which is available at wileyonlinelibrary.com.]

reactors have been modeled using various approaches such as Monte–Carlo method,[15,16] pseudo-homogeneous model with two-flux incident submodel,[7] rigorous three-dimensional diffusion-convection-reaction model[17] and two-dimensional heterogeneous convection-reaction model.[18] Most recently, computational fluid dynamics (CFD) has emerged as a popular tool for investigating the photoreactors.[19] Mohseni and Taghipour[20] investigated the flow field and photocatalytic reaction of air-borne vinyl chloride oxidation in an annular photocatalytic reactor using FLUENT. Pareek and Adesina[19] simulated the behavior of an annular photocatalytic reactor for the degradation of spent Bayer liquor using discrete ordinates (DO) radiation model. Salvado-Estivill et al.[21] coupled the radiation field with photocatalytic reaction kinetics for rigorous modeling of a single-pass flat-plate photocatalytic reactor for air purification. In recent times, Castrillon and de Lasa[6,14] used another CFD code CFX for simulating the photo-CREC-air proposed by de Lasa and Ibrahim.[22] Denny et al.[13] simulated the photocatalytic degradation of oxalic acid in a glass-bead photoreactor irradiated by optical fibers.

It is well known that honeycomb monolith reactors offer low-pressure drop and high-catalyst surface area.[23] Mazumder and Sengupta[24] conducted a rigorous subgrid scale CFD simulation on heterogeneous catalytic reactions occurring in a set of porous or honeycomb monoliths. However, previous studies have only dealt with high-temperature catalytic reactions in which the radiation was not involved,[24] or for modeling only a single channel of a monolith.[8,9,16,17] Hossain et al.[17] simultaneously modeled flow field, radiation, and kinetics of toluene and formaldehyde degradation through a single monolith channel. By assuming that all channels in a monolith had same flow and radiation field, and there was no entrance effect, they then calculated conversion profiles for the degradation of these chemicals. They achieved a good agreement between their model predictions and experimental values for both pressure drop and conversion profiles. However, as indicated by the authors, the uniform velocity assumption can introduce errors in calculations particularly at low Reynolds numbers.

Optimizing a monolith photocatalytic reactor is not trivial as there exists a complex interaction between the fluid flow, monolith and lamp spacing, and light intensity distribution. Therefore, in this study, to account for all these parameters simultaneously, we have conducted a CFD simulation on a full-scale honeycomb monolith reactor for photodegradation of toluene and formaldehyde. The DO radiation model was chosen for the radiation field, whereas FLUENT's species transport model and Langmuir–Hinshelwood (L-H) reaction kinetics were adopted for the photocatalytic oxidation reaction modeling. The feature of this novel approach was that the monoliths were treated as porous and highly absorbing zones and were coupled with the simplified radiative transfer equation (RTE) by introducing an adjustable parameter—the absorption coefficient of the channel wall in the equation. In addition, a user-defined function (UDF) was used to describe the L-H kinetics, which was also a function of the local UV flux inside the monoliths. Using this modeling approach, the photocatalytic degradation of toluene and formaldehyde was evaluated and compared with the experimental results from Hossain et al.[17] Additionally, the effects of light intensity and reactor wall reflectivity on the reactor performance were investigated.

Experimental Details

The experimental data were taken from the studies of Hossain et al.[17] In the study, a pilot scale demonstration unit was used to examine the photodegradation of toluene and formaldehyde. The pilot unit was 2.4-m long, 0.3 m × 0.3 m cross-sectional duct, and could accommodate up to six lamp banks (each consisted of four UV lamps) and five square honeycomb monoliths (see Figure 1, for an example of a reactor consisting of six lamp banks and five monoliths). The reactor wall was made of compressed fiber glass and the inner duct wall was covered by aluminum foil to reflect the light. The reactor elements were alumina ceramic foams (HiTech) and low-pressure mercury lamps were used (Voltrac G10T5L-S400). The ceramic foams were 64 cells per square inch (CPSI) and wash-coated with Degussa P25 titania (5% by weight of titania in distilled water) to yield a thickness of 20 μm. UV coming from the mercury lamps was emitted at 254 nm. A UVC power meter (Oriel UVC Goldilux) was used to measure the UVC intensity at the monolith faces.

Unfiltered building air was blown into the reactor to provide the desired flow. The contaminants, formaldehyde and toluene were introduced through a diffusion-controlled vaporizer and a compressed gas cylinder supply, respectively. The concentration measurements of formaldehyde and water vapor were carried out by a Brüel & Kjaer 1302 multigas monitor, whereas the concentration of toluene was measured by a gas chromatograph (IBM-9630) equipped with a 10% carbowax 20-M Chrom WAW 80-100-M packed column and a flame ionization detector (FID). The absolute concentration uncertainties were estimated to be ± 0.020 ppm$_v$ and ± 0.010 ppm$_v$ for formaldehyde and toluene, respectively. Note that the above experimental details were extracted from Hossain et al.[17]

Model Development

The regular-shaped monoliths in the reactor were simulated as porous zones in FLUENT. The following general assumptions were made: (1) the system was in a steady state isothermal condition; (2) the flow was laminar and incompressible; (3) there were negligible absorption, scattering or emission of radiation by the gaseous medium[17]; (4) the monolith channels were adiabatic and nonconducting; (5) the diffusion coefficient was constant; (6) no homogeneous chemical reaction occurred; and (7) the coatings on the monoliths were suitably thick and uniform so there was no transmission of light.[17]

Radiation field model

The generic RTE may be expressed as:

$$\frac{dI_v(\mathbf{s},\Omega)}{d\mathbf{s}} + \kappa_v I_v(\mathbf{s},\Omega) + \sigma_v I_v(\mathbf{s},\Omega) - \frac{1}{4\pi}\sigma_v \int_{4\pi} p(\Omega' \longrightarrow \Omega) I_v(\mathbf{s},\Omega') d\Omega' = 0. \quad (1)$$

The second term on the left hand side symbolizes the loss of photons due to absorption; the third term accounts for the loss of photons due to out-scattering; the last term indicates the in-scattering of photons. Since there was no scattering, absorption or emission by the gaseous medium (outside the monolith channels), both scattering and absorption coefficients were zero and Eq. 1 reduces to:

$$\frac{dI_v(\mathbf{s},\Omega)}{d\mathbf{s}} = 0 \qquad \text{(for outside the channels).} \qquad (2A)$$

However, for inside the monolith channels, there is gradual loss of light due to the absorption by the channel wall. Therefore, by introducing the absorption coefficient of the channel wall $\kappa_{\upsilon,\text{channel}}$, and assuming that the scattering is negligible compared to the absorption, Eq. 1 simply reduces to Eq. 2B, which closely resembles the Beer–Lambert's law for light transmission through a nonscattering medium:

$$\frac{dI_v(\mathbf{s},\Omega)}{d\mathbf{s}} + \kappa_{\upsilon,\text{channel}} I_\upsilon = 0 \qquad \text{(for inside the channels).} \qquad (2B)$$

The absorption coefficient of the channel wall, $\kappa_{\upsilon,\text{channel}}$ in Eq. 2A was estimated by a trial-and-error approach and Eqs. 2A and 2B were then solved using the DO radiation model. In this model, the radiation field is divided into a finite number of volumes and discrete solid angles and Eq. 2 is solved spatially and directionally. In other words, Eq. 2 is integrated over both the control angle and the control volume.[25] An angular discretization of 6 × 6 was used in this study, which means an octant of the angular space was discretized into a finite number of polar and azimuthal control angles, i.e., $N_\theta \times N_\phi$. Therefore, for a three-dimensional modeling, a total of $8N_\theta N_\phi$ equations are solved for each wavelength band. The incident intensity at any point from all the directions is calculated using:

$$I_v(s) = \int_0^{4\pi} I_\upsilon(s,\Omega) d\Omega. \qquad (3)$$

Flow model, transport equation, and kinetics

It is more practical to model the individual monoliths by using porous media formulations instead of introducing computational grids, which are in the range of submicrons compared with the overall photoreactor.[24] FLUENT solves Navier–Stokes equations based on the assumptions of conservation of mass and momentum in a moving fluid. The conservation of mass and momentum are described in Eqs. 4 and 5, respectively. In addition, an additional species conservation equation, Eq. 6 is solved:

$$\frac{\partial(\varepsilon)\rho}{\partial t} + \nabla \cdot (\varepsilon\rho\boldsymbol{v}) = 0 \qquad (4)$$

$$\frac{\partial}{\partial t}(\varepsilon\rho\boldsymbol{v}) + \nabla \cdot (\varepsilon\rho\boldsymbol{v}\boldsymbol{v}) = \nabla \cdot \varepsilon(\overline{\overline{\tau}}) + \varepsilon\rho\mathbf{g} + \mathbf{S_M} \qquad (5)$$

$$\frac{\partial}{\partial t}(\varepsilon\rho Y_i) + \nabla \cdot (\varepsilon\rho\boldsymbol{v}Y_i) = -\nabla \cdot \mathbf{J_i} + R_i \qquad (6)$$

where ε is the bulk porosity which was taken as 0.5.[8] $\mathbf{S_M}$ is the momentum sink term (N/m^3), which includes the pressure drop due to the photocatalyst support and the monolith channels. Since the monoliths are modeled as porous zones, the monoliths can then be characterized by a bed of particles. For laminar flow through the porous bed,

$$-\mathbf{S_M} = \left(D\mu + C_2\frac{1}{2}\rho|\boldsymbol{v}|\right)\boldsymbol{v}, \qquad (7)$$

where the first term on the right-hand side accounts for viscous loss (Darcy's) and the second term accounts for inertia loss. D and C_2 are the user inputs, where

$$D = \frac{1}{\alpha}, \qquad (8)$$

$$\alpha = \frac{D_\text{P}^2}{150}\frac{\varepsilon^3}{(1-\varepsilon)^2}, \qquad (9)$$

$$C_2 = \frac{3.5}{D_\text{P}}\frac{(1-\varepsilon)}{\varepsilon^3}. \qquad (10)$$

By approximating the capillary of flow through cylindrical pores, the particle diameter (D_P) can then be expressed in terms of the specific surface of the monolith, a_V by[26]:

$$D_\text{P} = \frac{6(1-\varepsilon)}{a_V}. \qquad (11)$$

$\mathbf{J_i}$ in Eq. 6 is the mass diffusion in laminar flows,

$$\mathbf{J_i} = -\rho D_{i,m}\nabla Y_i, \qquad (12)$$

where $D_{i,m}$ is the diffusion coefficient for species i in the mixture for which a constant value of 2.88×10^{-5} m^2/s was used in the simulation to account for the diffusivity of the dilute concentration of VOCs in air.

R_i in Eq. 6 is the contaminant sink term, which is essentially the kinetic model of the oxidation rate of the VOCs. In this work, a bimolecular form of the L-H reaction rate was used to model the reaction rates of toluene and formaldehyde conversions at constant humidity. The correlation coefficients

Table 1. L-H Correlation Coefficients[27]

Gas/Adsorption Coefficient	K_0	K_1	K_2	K_3	K_4
Toluene	0.34	1.93	0.00036	1.93	0.00036
Formaldehyde	1.05	1.02	0.00020	1.11	0.015

were extracted from Obee,[27] who by making an assumption that the contaminant and water vapor were the only important factors in the reaction rates, simplified the L-H rate equation:

$$-R_i = K_0' \frac{K_1 X_C}{1 + K_1 X_C + K_2 X_W} \frac{K_4 X_W}{1 + K_3 X_C + K_4 X_W}, \quad (13)$$

where X_C and X_W are the concentrations of the contaminant and water in ppm$_v$, respectively, and K_1,K_2,K_3 and K_4 are the Langmuir adsorption constants in ppm$_v{}^{-1}$. The corresponding reaction constants are given in Table 1. K_0' (μmol cm^{-2} h^{-1}) is the rate constant accounting for the effect of local UV flux I incident on the monolith walls and is evaluated using the following empirical equation:

$$K_0' = K_0 \left(\frac{I}{I_G} \right)^{0.5}, \quad (14)$$

where I_G is the UV flux for which the kinetic constants were evaluated.[17,27] The local UV flux I is evaluated using Eq. 2B. In general, the photocatalytic reaction rate is proportional to I^α, with α being 1 or 0.5 for low- or high-intensity radiation, respectively.[28] According to Obee and Brown,[29] the oxidation rate of formaldehyde and toluene on a monolith was a power law function of the UV intensity with an exponent of 0.55, subject to 0.05 uncertainties in the exponent.[29] Therefore, in this study, an exponent of 0.5 was chosen for both toluene and formaldehyde degradations. To enable the volumetric reactions in the porous media, Eq. 13 is thus converted to Eq. 15 to volumetric reaction rate by multiplying it with the illuminated specific area of the photocatalysts (a_λ):

$$-R = K_0' \left(\frac{K_1 X_C}{1 + K_1 X_C + K_2 X_W} \right) \left(\frac{K_4 X_W}{1 + K_3 X_C + K_4 X_W} \right) a_\lambda. \quad (15)$$

Equations 14 and 15 are then compiled using a set UDF to describe the degradation processes.

Boundary conditions

The following boundary conditions were employed: (1) a uniform inlet air velocity (due to the placement of some airflow-straightened elements at the upstream and downstream of the monoliths[30]); velocity and concentration of the contaminants were set according to the experimental tests; (2) a pressure-specified outlet boundary condition, with gauge pressure at 0; (3) a "porous jump" boundary condition at the interfaces between monolith blocks and fluid; (4) a diffuse semitransparent wall for the UV lamp surfaces; and (5) a diffusely reflecting aluminum wall for the reactor wall.

Results and Discussions

Computational domain and solver parameters

The experiments carried out by Hossain et al.[17] had one to five honeycomb monoliths. The mean UV flux on the monolith surfaces was 60–65 W/m^2 and the airflow rates ranged between 0.0260 and 0.1935 m^3/s (i.e., 55–410 ft^3/min).[17] Figure 1 shows the photoreactor with five monoliths and six lamp banks. The lamp banks were placed parallel to the monoliths, and each bank consisted of four lamps.

A segregated, pressure-based solver was used and the calculations were performed until the species and intensity residuals reached steady values. A typical convergence history required about 2500 iterations on a processor of AMD Opteron™ Processor 252.

Light intensity distribution

Hossain et al.[17] plotted the dimensionless wall flux profile for a single monolith channel of aspect ratio equal to 8 as a function of the axial distance, and found that the UV flux falls to less than 10% and 1% of the incident wall flux at reduced distances of one and three, respectively. A reduced distance is a dimensionless term and is defined as the axial coordinate divided by the width of a single monolith channel/pore. Therefore, a monolith of 2.54 cm (1 inch) in depth having an average channel diameter of 0.3175 cm can be divided into a total of 8 reduced distances. Beyond the reduced distance of three, the monolith channels receive very little light.[17] Besides, due to the shadows cast by the incoming light at the entrance of the monolith, the wall flux at the

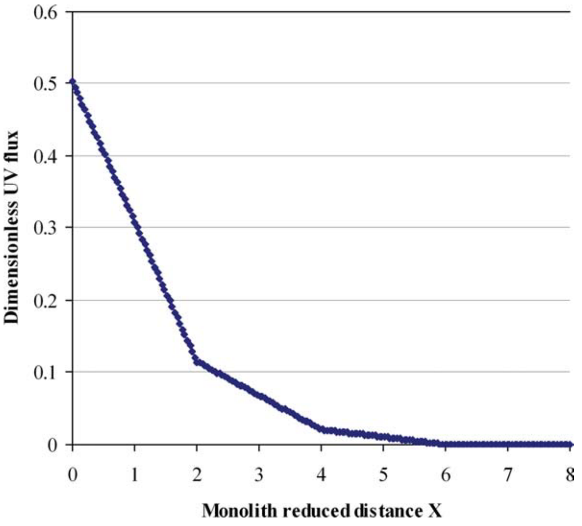

Figure 2. Dimensionless UV flux profile across a single-faced irradiated monolith.

[Color figure can be viewed in the online issue, which is available at wileyonlinelibrary.com.]

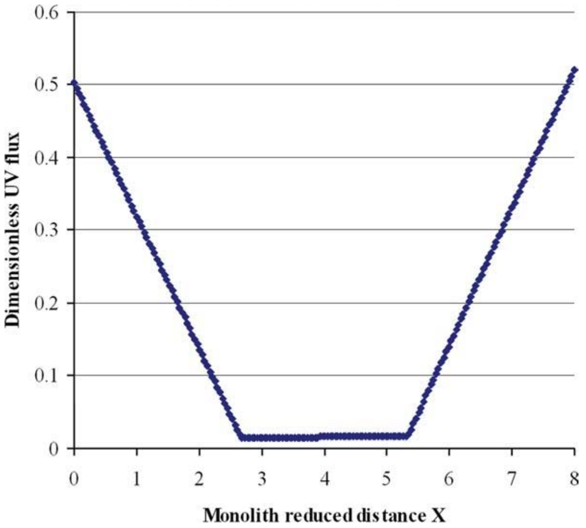

Figure 3. Dimensionless UV flux profile across a double-faced irradiated monolith.

[Color figure can be viewed in the online issue, which is available at wileyonlinelibrary.com.]

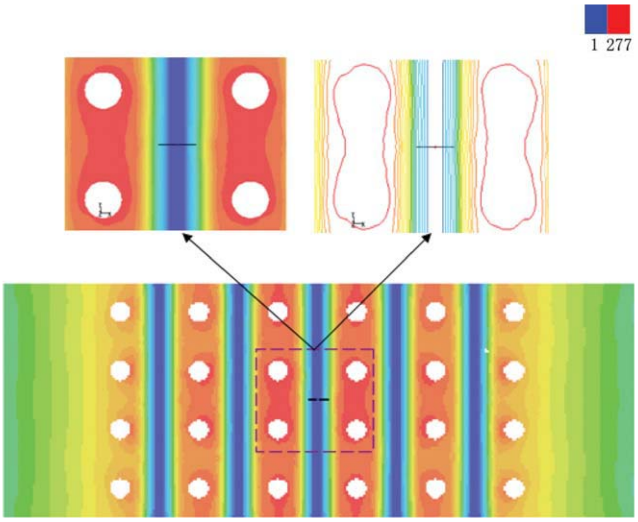

Figure 4. UV flux contour on the center plane.

[Color figure can be viewed in the online issue, which is available at wileyonlinelibrary.com.]

monolith inlet is only half that of the incident flux on the outer surface of the monolith, due to the phenomenon known as the ballistic transport.[17] Using these observations, by trial and error, the parameter $k_{v,\ \mathrm{channel}}$ in Eq. 2B was estimated as 10^6 m^{-1}.

Figure 2 shows the UV flux across a single-faced irradiated monolith as a function of the axial coordinate. Because the irradiation emanating from the lamp bank located in front of the monolith, the UV flux is the highest at the monolith inlet, and rapidly declines to 30% of the incoming flux at a reduced distance of one and to 1% of the incoming flux at a reduced distance of three. There are some deviations in the predicted UV flux profile compared to the experimentally measured UV flux (20% disparity at the reduced distance of one), which can potentially be rectified by using one more model parameter for the ballistic transport.[17] This drastic decline in light intensity highlights the major drawback of a monolith photoreactors, in which the photocatalyst-coated monolith walls absorb most of the incident light and causes nearly dark conditions after a reduced distance of three.

As shown in Figure 3, for a double-faced irradiated monolith, the UV flux was distributed in a parabolic manner, due to the irradiation emanating from the two lamp banks located ±2.5 cm away from the monolith. Placement of lamp banks on both sides of the monolith reduces the dark zones, thereby improving the distribution of light intensity on the surfaces of the monolith. Furthermore, as seen in Figure 3, the illuminated fraction of a double-faced irradiated monolith

Table 2. Operating Conditions of Different Tests for (a) Toluene Degradation and (b) Formaldehyde Degradation[17]

Test no.	Flow Rate $\times 10^{-2}$ (m^3/s)	UV Flux (W/m^2)	Inlet Conc. (ppm_v)	Water Conc. (ppm_v)	Lamps/Irradiated Monolith Faces	Monolith Length (cm)	Measured Conversion (%)	Predicted Conversion (%)	Error (%)
(a) Toluene degradation									
1	2.97	65	0.30	3500	24/10	2.54	68	67.4	0.8
2	9.91	65	0.10	3500	24/10	2.54	38	32.7	13.8
3	19.35	65	0.05	3500	24/10	2.54	22	19.5	11.5
4	9.91	65	0.30	3800	24/10	2.54	26	26.6	−2.4
5	2.97	65	0.30	5800	24/10	2.54	62	65.9	−6.2
6	3.26	65	0.36	2200	24/10	2.54	62	57.7	6.9
(b) Formaldehyde degradation									
7	9.44	65	0.4	3900	8/4	2.54	50	52.2	−4.4
8	9.44	65	0.4	3900	16/8	2.54	82	81.0	1.3
9	19.35	65	0.3	2800	8/4	2.54	24	33.7	−40.6
10	2.60	65	1.9	6000	4/1	2.54	44	31.7	28.0
11	2.60	65	1.9	6000	4/2	2.54	77	54.4	29.4
12	2.60	65	2.1	2700	4/1	1.27	35	22.4	36.1
13	2.60	65	2.1	2700	4/2	1.27	52.5	55.3	−5.4
14	2.60	65	2.1	2700	4/1	2.54	42.5	34.6	18.6
15	2.60	65	2.1	2700	4/2	2.54	60.5	57.7	4.6
16	2.60	65	2.1	2700	4/1	3.81	43.5	34.5	20.8
17	2.60	65	2.1	2700	4/2	3.81	66	57.8	12.5
18	9.44	65	0.7	4800	8/4	2.54	54	46.2	14.4
19	19.35	65	0.3	2800	24/10	2.54	60	69.4	−15.6

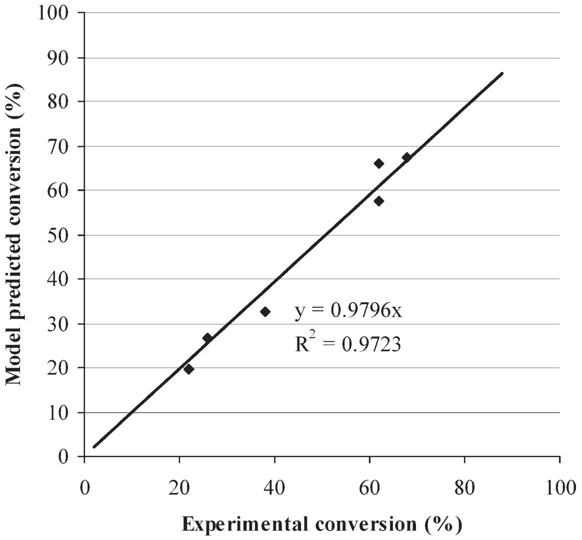

Figure 5. Comparison between model and experimental conversions for toluene degradation.

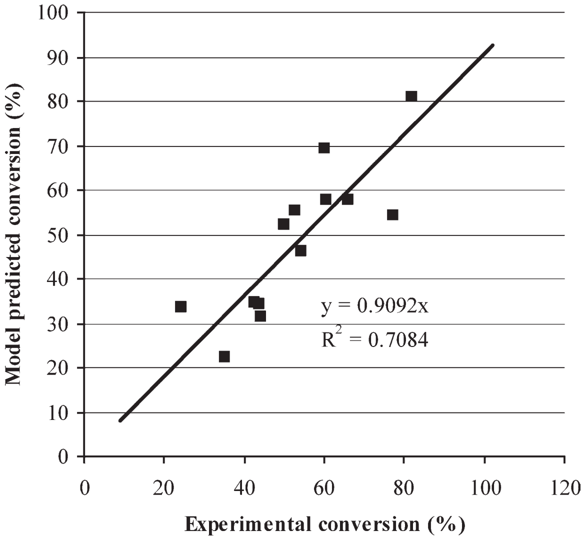

Figure 6. Comparison between model and experimental conversions for formaldehyde degradation.

occupies ~10% of the total volume. Therefore, the illuminated specific area (or the effective specific area) in Eq. 14 was taken to be 10% and 5% of the total specific area for the double-faced and single-faced irradiated monoliths, respectively.

A general view of the UV flux contour on the center plane of the monolith reactor is shown in Figure 4. The color changes of the UV flux contour show that the highest UV flux happens at the lamp surfaces, it then progressively decreases with the axial distance to 65 W/m^2 at the monolith's inlets and outlets. Subsequently, the UV flux incident on the monoliths is allowed to follow the UV flux profiles as shown in Figures 2 and 3. Likewise, the enlarged portions in Figure 4 show the UV flux trends in the transverse *y*-direction.

Model validation

The simulation results were validated against the experimental data from the pilot-scale demonstration of Hossain et al.[17] The simulation runs were conducted according to different reactor layouts and operating conditions of the experiments. A total of 19 cases were compared (6 cases for toluene and 13 for formaldehyde). Table 2 shows the experimental details and model results for different runs. The flow rates ranged from 0.0260 to 0.1935 m^3/s, and the measured mean UV flux on the 30.48 cm × 30.48 cm monolith surfaces was 65 W/m^2. It is important to note that all the flow rates were chosen such that the reactor remained kinetically controlled.[17] For example, take test 1 as an assessment case;

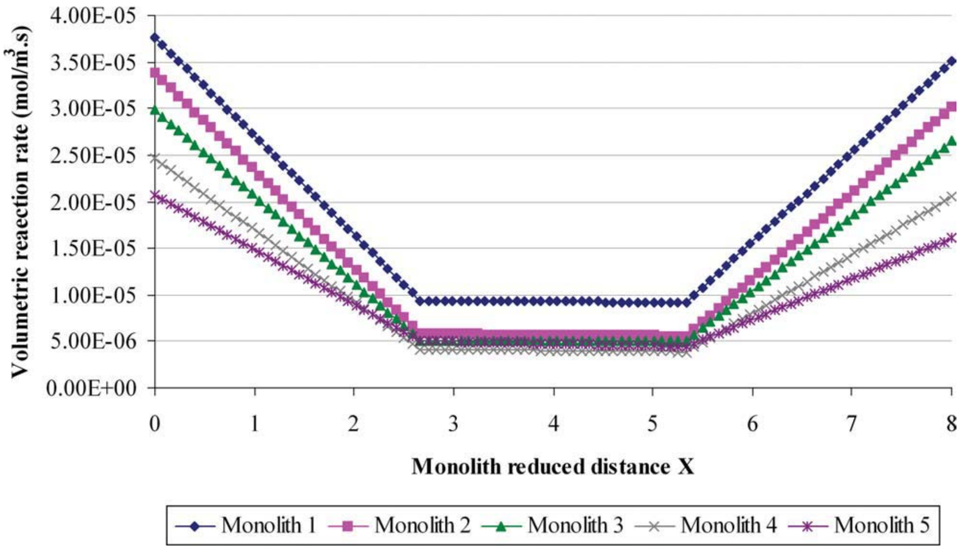

Figure 7. Reaction rate profiles of toluene degradation in Test 1 across the center line.

[Color figure can be viewed in the online issue, which is available at wileyonlinelibrary.com.]

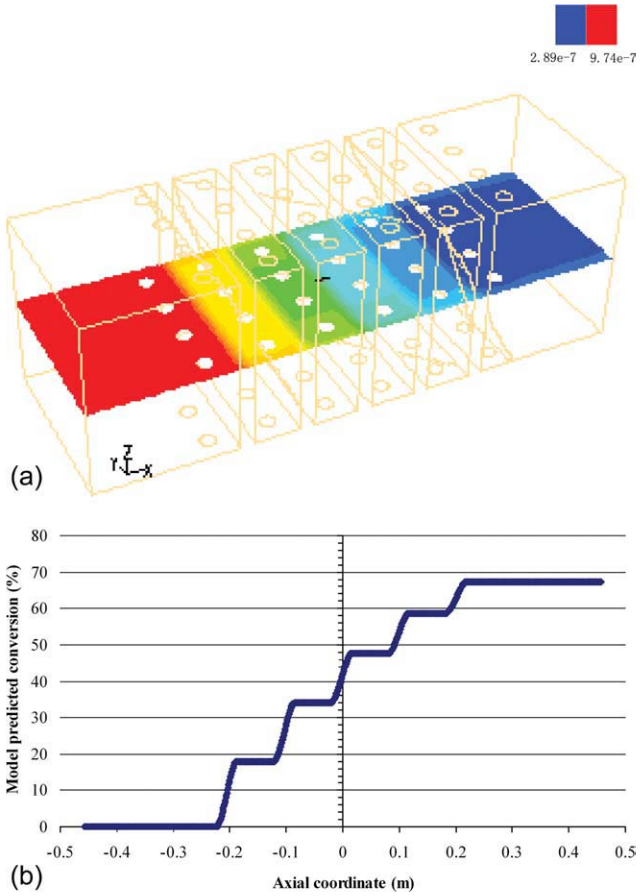

Figure 8. (a) Mass fraction contour of toluene in Test 1; and (b) area-weighted average mass fraction profile across the center plane (z = 0).

[Color figure can be viewed in the online issue, which is available at wileyonlinelibrary.com.]

inlet air consisting of 0.3 ppm$_v$ toluene and 3500 ppm$_v$ water vapor was introduced at flow rate of 00297 m^3/s to the monolith reactor which contained five double-faced irradiated monoliths of length 2.54 cm and six lamp banks. The measured conversion of toluene was 68%, whereas the predicted conversion was 67.4%, with an error percentage of 0.8.

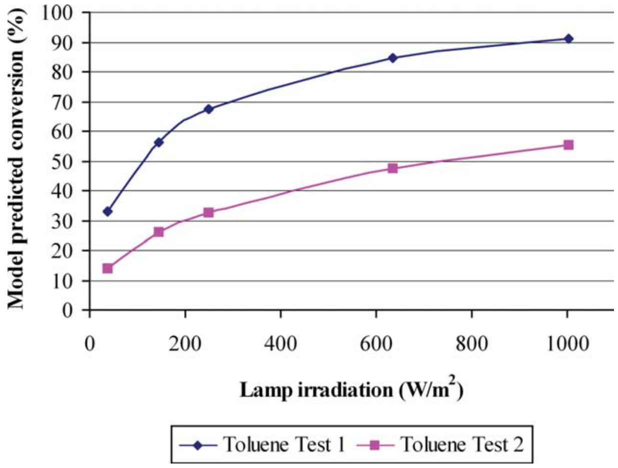

Figure 10. Conversion dependence on lamp irradiation for Tests 1 and 2.

[Color figure can be viewed in the online issue, which is available at wileyonlinelibrary.com.]

Figures 5 and 6 show graphical comparisons of the model and experimental results for toluene and formaldehyde degradation, respectively. y-Axis is the conversion predicted by the model and x-axis is the measured/experimental conversion. The locations of the data points determine the accuracy of the model data. The ideal case happens when all the data points fall on the diagonal of the plot. As seen in Figure 5, for toluene degradation, the slope of the best-fit line for the data points is 0.98, with R^2 of 0.97. The model-predicted results successfully matched the experimental results.

For formaldehyde conversions, as shown in Figure 6, the slope of the best-fit line is 0.91, with R^2 of 0.71. The slope and R^2 values are lower compared to those of toluene conversions. Some possible reasons for the mismatch are attributed to the failure of the bimolecular L-H correlation in predicting the oxidation rates subject to different humidity in the system.[29] Another reason could be the temperature effect. From the studies of Obee and Brown,[29] a temperature rise of 20°C caused the oxidation rate of formaldehyde to decrease by 10% but had no impact on the oxidation rate of toluene. Nonetheless, the good agreement between the results predicted by the model and those obtained in the experiment

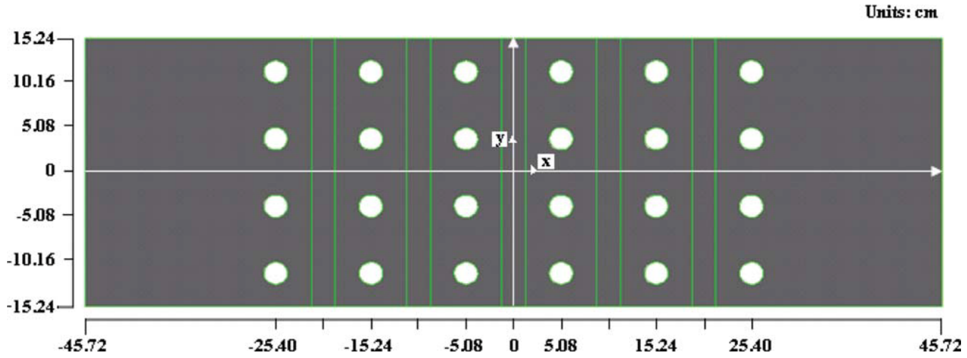

Figure 9. Coordinate system for the monolith reactor modeling.

[Color figure can be viewed in the online issue, which is available at wileyonlinelibrary.com.]

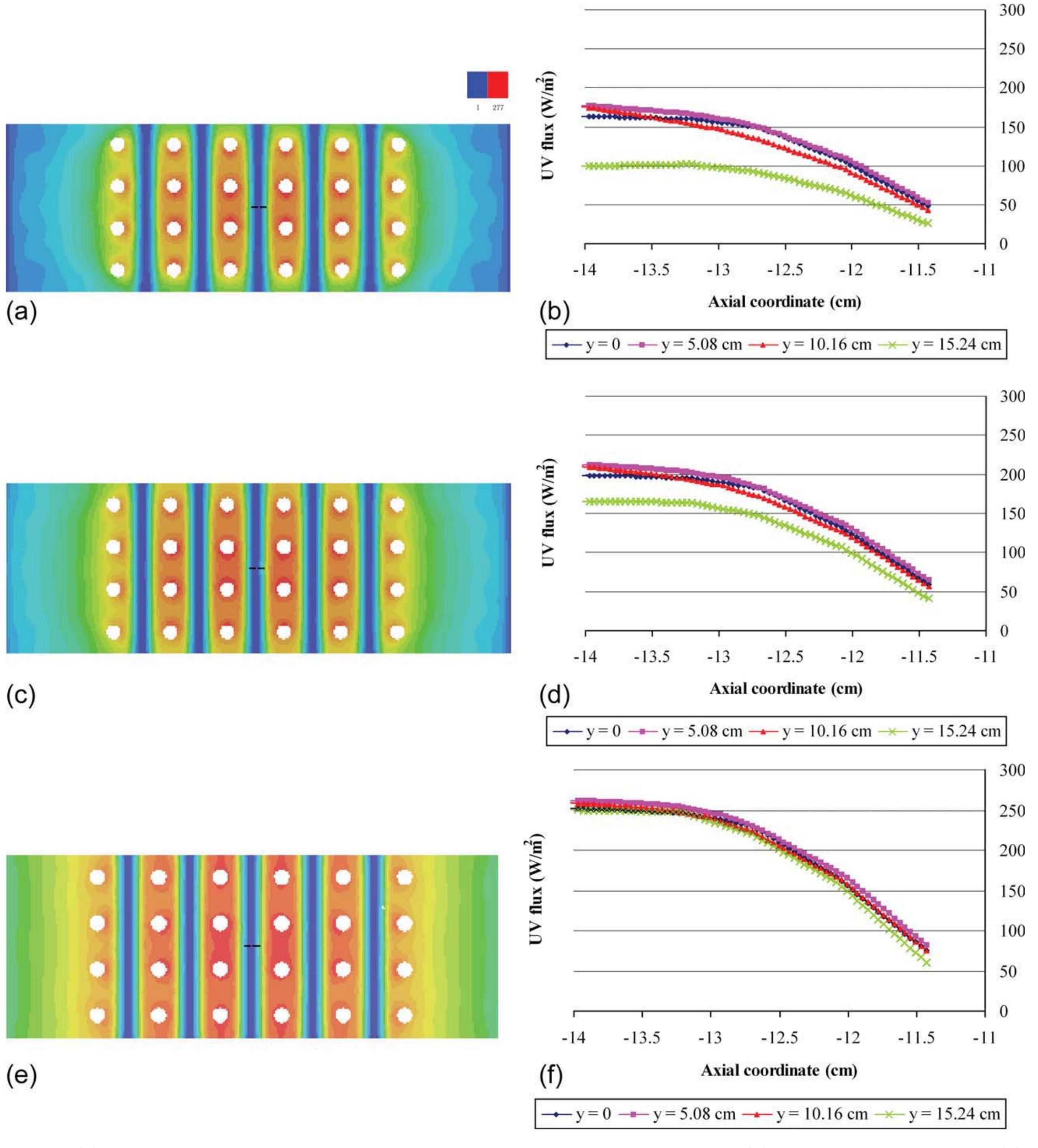

Figure 11. (a) UV flux contour on the center plane for reactor wall reflectivity r = 0; (b) UV flux profile for r = 0; (c) UV flux contour on the center plane for reactor wall reflectivity r = 0.5; (d) UV flux profile for r = 0.5; (e) UV flux contour on the center plane for reactor wall reflectivity r = 0.98; and (f) UV flux profile for r = 0.98.

[Color figure can be viewed in the online issue, which is available at wileyonlinelibrary.com.]

for both cases reveal that the novel approach presented in this article is a good ‘‘vehicle’’ to describe the photocatalytic oxidation of VOCs in a honeycomb monolith reactor.

VOCs degradation

Again, taking Test 1 as an assessment case, Figure 7 shows the reaction rate profiles of toluene degradation in this test across the centerline of each of the monoliths in the reactor. Monolith 1 is the first reaction space that the contaminated air encounters and thus has the highest rate of chemical reaction. It can be seen that the reaction rate slightly decreases for the subsequent monoliths with the last monolith (monolith 5) having the lowest values of reaction rates. Most notably, the reaction rate profiles follow the trend of

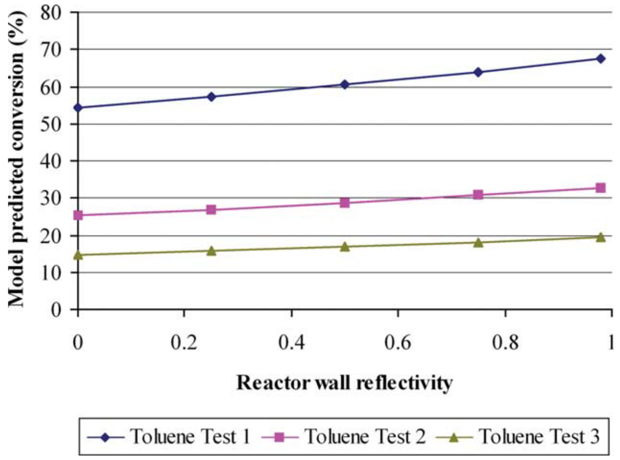

Figure 12. Conversion as a function of the reactor wall reflectivity for Tests 1, 2, and 3.

[Color figure can be viewed in the online issue, which is available at wileyonlinelibrary.com.]

UV light flux shown in Figure 3, in which the highest reaction rates occur at the monolith's inlet ($X = 0$) and outlet ($X = 8$), where the incident light intensity is the highest. Moreover, it shows that the lower the intensity of the light flux, the lower the value of the reaction rate. This result signifies the importance of integrating the local UV flux into the kinetics or reaction rates.[21]

Figure 8a shows a mass fraction contour of toluene in Test 1 across the center plane ($z = 0$) from the reactor inlet to the outlet. The changes in color of the center plane happen after each monolith, implying the decrease in toluene mass fraction due to the photocatalytic oxidation reactions occurring inside the monolith, i.e., in the porous zones. Figure 8b shows the toluene conversion profile in the axial direction on the center plane in Figure 9. It is clear that the conversion of toluene takes place in the porous zones in a step-stair manner. For example, the conversion of toluene is 18% after monolith 1, and increases to 33% after monolith 3, and eventually to 67% when the air stream exits the monolith. Therefore, the desired conversion can be achieved by increasing the number of monoliths in the reactor. However, increasing the number of monoliths requires higher energy usage to power the UV lamps. Therefore, a trade off must be made in deciding the number of lamps and monoliths by taking into consideration energy utilization and process economics.[31]

Effect of light intensity

In this study, a constant aspect ratio of 8 was used and the dependence of VOC conversion on the lamp irradiation for Tests 1 and 2 is plotted in Figure 10, which shows that the extent of degradation was the first-order at lower intensities and followed a power law of exponent 0.5 at higher intensities. This result is consistent with the findings of Yu et al.[32] Using this plot, one can choose the optimum UV lamp irradiation for the photocatalytic reactions by balancing the energy usage and conversion of VOCs.

Effect of reactor wall reflectivity

Since the reaction mixture was essentially air without any solids, the absorption, scattering, and emission of radiation by the medium outside the monoliths was negligible. For such an optically thin system, the reflectivity of reactor walls is likely to play an important role. We also note that here the wall reflectivity refers to the enclosing reactor walls not the monolith walls. Figures 11 shows the contours and the corresponding profiles of the UV flux from the lamp surface to the monolith surface ($x = -13.97$ cm to -11.43 cm, at various y-coordinates, with the coordinate system being as shown in Figure 9) for different values of reactor wall reflectivity. Analyzing Figures 11a, b, for the reactor with nonreflective wall ($r = 0$, which also means that the wall is completely absorptive), the peak intensity was at the lamp surface (~153 W/m^2). The intensity then rapidly diminishes to 83% of the original flux at the midpoint between the lamps and the monolith surface, eventually falling to 35 W/m^2 at the monolith surface, which is only half of the UV flux used in the experiments. Besides, the UV flux at the reactor wall ($y = 15.24$ cm) has the lowest value compared to those at other transverse positions, due to the nonreflective nature of the reactor wall. On the other hand, Figures 11c, d show a relatively uniform light distribution throughout the space when the reactor wall is partially reflective ($r = 0.5$, i.e., half of the light incident is reflected with the remainder

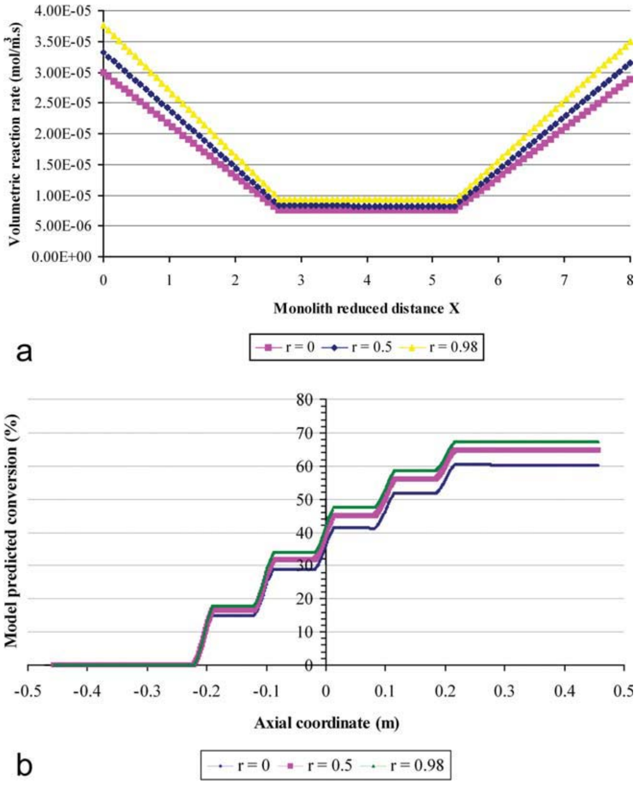

Figure 13. (a) Reaction rate dependence on reactor wall reflectivity across the center line of monolith 1 in Test 1; and (b) conversion in Test 1 for different reactor wall reflectivities.

[Color figure can be viewed in the online issue, which is available at wileyonlinelibrary.com.]

being absorbed). At the midpoint between the lamps and monolith surface, the UV flux falls to 88% of the original flux, finally decreasing to 47 W/m^2 at the monolith surface. Thus, the UV flux at the monolith's surface improves by $\sim$18% when a partially reflective reactor wall is used.

Figures 11e, f show the UV fluxes when the reactor wall was nearly completely reflective ($r = 0.98$ in this case). It is clear that with these highly reflective reactor walls, the light intensity distribution within the reactor greatly improves. In this case, at the midpoint between the lamps and the monolith surface, the UV flux decreases slightly to 92% of the original flux and eventually to 65 W/m^2 at the monolith surface. This suggests that reactor wall reflectivity plays a considerably important role for this reactor system, and that a completely reflective reactor wall is preferable to obtain a much uniform light distribution.

Figure 12 shows that the conversion also increases with the reactor wall reflectivity. In addition, Figure 13 shows the reaction rate and conversion profiles across the monolith in the axial direction for nonreflective, partially reflective, and completely reflective walls. As can be seen in Figure 13a that the completely reflective reactor wall provides the highest reaction rate, followed by a partial reflective one, which provides $\sim$10% lower reaction rate, and lastly the nonreflective reactor wall provides $\sim$20% lower reaction rate compared to the completely reflective wall. This difference consequently affects the conversion of the VOCs. Figure 13b shows that an overall 67% conversion is achieved when a completely reflective reactor wall is used, and conversions of 61% and 54%, respectively, are achieved when the partially reflective and nonreflective reactor walls are used. Therefore, it is evident that for a system of this nature, reactor wall reflectivity plays a substantial role in the distribution of light, which in turn, influences the effectiveness of the photodegradation of the VOCs. Certainly, employing a completely reflective reactor wall would be at the expense of higher material and manufacturing costs, as well as the fouling of the reactor surface over the period may reduce the reflectivity, thus require periodic cleaning.

Conclusion

A semiempirical CFD modeling approach for the photocatalytic degradation of toluene and formaldehyde in a honeycomb monolith photoreactor was presented. This approach treated the monoliths in the reactor as porous media and coupled with the simplified RTE to capture the local light flux by introducing an adjustable parameter, which was the absorption coefficient of the channel wall ($\kappa_{\upsilon,\mathrm{channel}}$). In addition, the L-H kinetics, which was also a function of the local UV flux inside the monoliths, was integrated into the radiation model to describe the photodegradation processes. The modeling data matched the published experimental results considerably well, thus confirming the reliability of this novel approach.

This approach offers simplicity at the same time provides visualization of the fluid flow, light intensity, and species distributions inside the entire reactor. The drawback of this approach was that a trial-and-error attempt was required to obtain the correct sink term (i.e., $\kappa_{\upsilon,\mathrm{channel}}\ I_{\upsilon}$) for the light intensity profile. Nonetheless, this article has shown the benefits and limitations of applying FLUENT radiation model in a light-absorbing porous medium. Apart from that, by plotting the conversion profile with respect to radiation intensity, one can choose the optimum number of lamps for the photocatalytic reactions. The model also predicted that the reactor wall reflectivity had considerable effect on the reaction rate and overall conversion, and a completely reflective reactor wall would enhance the light distribution inside the reactor.

Acknowledgments

We authors wish to thank CRC CARE for the financial support for this study. We are grateful to the anonymous reviewers for their helpful comments which have greatly improved this manuscript.

Notation

ρ = density (kg/m^3)
μ = dynamic viscosity (kg/m s)
λ = wavelength (m)
α = permeability
ε = porosity
$\bar{\bar{\tau}}$ = stress tensor
σ = scattering coefficient (1/m)
σ_ν = spectral scattering coefficient (1/m)
κ = absorption coefficient (1/m)
κ_ν = spectral absorption coefficient (1/m)
$\kappa_{\nu,\mathrm{channel}}$ = monolith channel spectral absorption coefficient (1/m)
Ω = solid angle
$p(\Omega' \rightarrow \Omega)$ = phase function
D_p = bed particle diameter (m)
$D_{i,m}$ = diffusion coefficient for species i (m^2/s)
I = radiation intensity (W/m^2)
I_ν = spectral radiation intensity (W/m^2)
J_i = species mass diffusion
p = pressure (Pa)
S_i = contaminant sink term (kg/m^3 s)
S_M = momentum sink term (N/m^3)
T = temperature (K)
X_C = contaminant concentration (ppm$_\mathrm{v}$)
X_W = water vapor concentration (ppm$_\mathrm{v}$)
Y_i = species mass fraction
g = gravity vector
$\mathbf{s}$ = unit vector
$\mathbf{v}$ = velocity vector (m/s)

Literature Cited

1. Lomborg B. *The Skeptical Environmentalist: Measuring the Real State of the World.* Cambridge, U.K.: Cambridge University Press, 2001.
2. Wan R. *Analysis on influencing factors of indoor air quality and measures of improvement on modern buildings*. In: *2nd International Conference on Bioinformatics and Biomedical Engineering*. Shanghai, China: iCBBE, 2008.
3. Doug. Sick building syndrome and what you can do about it. A Report by Calutech, Inc. Plus an Introduction to Snapcat. United States: Titania, Advanced Air Oxidation Technology, Snapcat TM, 2005.
4. Wang SB, Ang HM, Tade MO. Volatile organic compounds in indoor environment and photocatalytic oxidation: state of the art. *Environ Int*. 2007;33:694–705.
5. Ruddy EN, Carroll LA. Select the best voc control strategy. *Chem Eng Progr*. 1993;89:28–35.
6. Castrillon SRV, de Lasa HI. Performance evaluation of photocatalytic reactors for air purification using computational fluid dynamics (CFD). *Ind Eng Chem Res*. 2007;46:5867–5880.
7. Raupp GB, Nico JA, Annangi S, Changrani R, Annapragada R. Two-flux radiation-field model for an annular packed-bed photocatalytic oxidation reactor. *AIChE J*. 1997;43:792–801.
8. Hossain MM, Raupp GB. Radiation field modeling in a photocatalytic monolith reactor. *Chem Eng Sci*. 1998;53:3771–3780.

9. Hossain MM, Raupp GB. Polychromatic radiation field model for a honeycomb monolith photocatalylic reactor. *Chem Eng Sci*. 1999;54: 3027–3034.
10. Choi W, Ko JY, Park H, Chung JS. Investigation on TiO_2-coated optical fibers for gas-phase photocatalytic oxidation of acetone. *Appl Catal B: Environ*. 2001;31:209–220.
11. Wang W, Ku Y. The light transmission and distribution in an optical fiber coated with TiO_2 particles. *Chemosphere*. 2003;50:999–1006.
12. Danion A, Disdier J, Guillard C, Abdelmalek F, Jaffrezic-Renault N. Characterization and study of a single-TiO_2-coated optical fiber reactor. *Appl Catal B: Environ*. 2004;52:213–223.
13. Denny F, Scott J, Pareek V, Ding Peng G, Amal R. CFD modelling for a TiO_2-coated glass-bead photoreactor irradiated by optical fibres: photocatalytic degradation of oxalic acid. *Chem Eng Sci*. 2009;64:1695–1706.
14. Castrillon SRV, Ibrahim H, de Lasa H. Flow field investigation in a photocatalytic reactor for air treatment (Photo-CREC-air). *Chem Eng Sci*. 2006;61:3343–3361.
15. Spadoni G, Bandini E, Santarelli F. Scattering effects in photosensitized reactions. *Chem Eng Sci*. 1978;33:517–524.
16. Alexiadis A. 2-D radiation field in photocatalytic channels of square, rectangular, equilateral triangular and isosceles triangular sections. *Chem Eng Sci*. 2006;61:516–525.
17. Hossain MM, Raupp GB, Hay SO, Obee TN. Three-dimensional developing flow model for photocatalytic monolith reactors. *AIChE J*. 1999;45:1309–1321.
18. Changrani RG, Raupp GB. Two-dimensional heterogeneous model for a reticulated-foam photocatalytic reactor. *AIChE J*. 2000;46:829–842.
19. Pareek VK, Adesina AA. Light intensity distribution in a photocatalytic reactor using finite volume. *AIChE J*. 2004;50:1273–1288.
20. Mohseni M, Taghipour F. Experimental and CFD analysis of photocatalytic gas phase vinyl chloride (VC) oxidation. *Chem Eng Sci*. 2004;59:1601–1609.
21. Salvado-Estivill I, Hargreaves DM, Li Puma G. Evaluation of the intrinsic photocatalytic oxidation kinetics of indoor air pollutants. *Environ Sci Technol*. 2007;41:2028–2035.
22. Ibrahim H, de Lasa H. Kinetic modeling of the photocatalytic degradation of air borne pollutants. *AIChE J*. 2004;50:1017–1027.
23. Sauer ML, Ollis DF. Acetone oxidation in a photocatalytic monolith reactor. *J Catal*. 1994;149:81–91.
24. Mazumder S, Sengupta D. Sub-grid scale modeling of heterogeneous chemical reactions and transport in full-scale catalytic converters. *Combust Flame*. 2002;131:85–97.
25. Pareek V, Chong S, Tadé MO, Adesina AA. Light intensity distribution in heterogenous photocatalytic reactors. *Asia-Pacific J Chem Eng*. 2008;3:171–201.
26. Wu J, Yu B, Yun M. A resistance model for flow through porous media. *Transp Porous Media*. 2008;71:331–343.
27. Obee TN. Photooxidation of sub-parts-per-million toluene and formaldehyde levels on titania using a glass-plate reactor. *Environ Sci Technol*. 1996;30:3578–3584.
28. Pareek VK, Adesina AA. *Analysis of photocatalytically reactive systems: kinetic modeling and reactor design via computational fluid dynamics (CFD)*. In: Nalwa MA-MaH, editor. *Handbook of Photoreactor*, vol. 1. Stevenson Ranch, CA: American Scientific Publishers (ASP), 2003:345–412.
29. Obee TN, Brown RT. TiO_2 photocatalysis for indoor air applications: effects of humidity and trace contaminant levels on the oxidation rates of formaldehyde, toluene, and 1,3-butadiene. *Environ Sci Technol*. 1995;29:1223–1231.
30. Hodgson AT, Destaillats H, Sullivan DP, Fisk WJ. Performance of ultraviolet photocatalytic oxidation for indoor air cleaning applications. *Indoor Air*. 2007;17:305–316.
31. Singh M, Salvadó-Estivill I, Puma GL. Radiation field optimization in photocatalytic monolith reactors for air treatment. *AIChE J*. 2007; 53:678–686.
32. Yu H, Zhang K, Rossi C. Theoretical study on photocatalytic oxidation of VOCs using nano-TiO2 photocatalyst. *J Photochem Photobiol A: Chem*. 2007;188:65–73.

Manuscript received Feb. 24, 2009, and revision received Apr. 20, 2010.